Anomalous sea-ice reduction in the Eurasian Basin of the Arctic Ocean during summer 2010

By Yusuke Kawaguchi*[1], Jennifer K. Hutchings[2], Takashi Kikuchi[1], James H. Morison[3], and Richard A. Krishfield[4]

[1]Research Institute of Global Change, Japan Agency for Marine-Earth Science and Technology, Yokosuka, Kanagawa, Japan; [2]International Arctic Research Center, University of Alaska Fairbanks, Fairbanks, US; [3]Applied Physics Laboratory, University of Washington, Seattle, US; [4]Woods Hole Oceanographic Institution, Woods Hole, Massachusetts, US.

Abstract

During the summer of 2010 ice concentration in the Eurasian Basin, Arctic Ocean was unusually low. This study examines the sea-ice reduction in the Eurasian Basin using ice-based autonomous buoy systems that collect temperature and salinity of seawater under the ice along the course of buoy drift. An array of GPS drifters was deployed with 10 miles radius around an ice-based profiler, enabling the quantitative discussion for mechanical ice divergence/convergence and its contribution to the sea-ice reduction. Oceanic heat fluxes to the ice estimated using buoy motion and mixed-layer (ML) temperature suggest significant spatial difference between fluxes under first-year and multi-year ice. In the former, the ML temperature reached 0.6 K above freezing temperature, providing >60–70 W m^{-2} of heat flux to the overlying ice, equivalent to about 1.5 m of ice melt over three months. In contrast, the multiyear ice region indicates nearly 40 W m^{-2} at most and cumulatively produced 0.8 m ice melt. The ice concentration was found to be reduced in association with an extensive low pressure system that persisted over the central Eurasian Basin. SSM/I indicates that ice concentration was reduced by 30–40% while the low pressure persisted. The low ice concentration persisted for 30 days even after the low dissipated. It appears that the wind-forced ice divergence led to enhanced absorption of incident solar energy in the expanded areas of open water and thus to increased ice melt.

Key Words

Summer sea-ice reduction in Eurasian Basin/ Warming in surface boundary layer/ Ice divergence due to a low pressure system/ Ice-albedo feed back

1 Introduction

The Arctic Ocean has experienced a dramatic decrease in summer ice extent over the past few decades (Comiso et al., 2008). This decrease in sea-ice cover has been pronounced especially in the western Arctic Ocean such as the Chukchi Sea, Beaufort Sea and adjacent seas in the Amerasian Basin (e.g., Shimada et al., 2006; Perovich et al. 2007; 2008). However, in the August 2010, there was appreciably low ice concentration in the central Eurasian Basin that was the second lowest since 1992 (Fig. 1). The reduced ice concentration is associated with holes that appeared in the ice pack (Fig. 2a), that were not present in the other low ice concentration years. This decrease in the concentration could lead to additional solar radiation deposited in the upper ocean and further decrease in the concentration through ice albedo-feedback. Hence, mechanical divergence of ice drift is a possible trigger for the increased ice reduction because it forcibly enlarges the open water area. In this study, we investigate the ice concentration reduction found in the Eurasian Basin during the summer 2010 from the view point of the mechanical ice divergence.

From the special sensor microwave imager (SSM/I) imagery, the low ice concentration first emerged in the mid-July around the North Pole and Amundsen Basin, and subsequently spread over the whole Eurasian Basin throughout August and early September. The concentration reduced by nearly 50% at greatest in late August and expanded extensively in the basin (Fig. 2a). The region of reduced ice concentration was centered on the Nansen-Gakkel Ridge (N-GR), which is located roughly 86.5°N, 30°E. The SSM/I images show the distinct difference in the concentration between the reduced-ice central Eurasian Basin and the packed ice region north of the Greenland. The low ice concentration in the Eurasian Basin was restored to 100% by the mid-September.

This paper aims to reveal what led to such prominent reduction in ice area of Eurasian Basin. We have analyzed temperature and salinity of the upper ocean collected by automated profiling instruments deployed on multiyear ice floes. The instruments that were tethered to the ice-mounted surface unit were deployed near the North Pole in the mid-April 2010 in conjunction with the North Pole Environmental Observatory (NPEO) program. One of the instruments is the Polar Ocean Profiling System (POPS) deployed by the Japan Agency for Marine-Earth Science and Technology (JAMSTEC), and another is the Ice Tethered Profiler (ITP) (Krishfield et al., 2008; Toole et al., 2006) deployed by Woods Hole Oceanographic Institution, which is identified as ITP#38. The two buoys drifted in the Amundsen and Nansen Basins with similar pathways; they traveled along the Lomonosov Ridge toward Greenland in June, and then changed direction to across the ridge joining the Transpolar Drift Stream (Fig. 2a). As the buoys traveled, they skirted the boundary region between the packed-ice in the north of Greenland and the most reduced-ice in the Eurasian Basin. In addition to these ice-based oceanographic profilers, 4 GPS drifters were deployed aside the POPS buoy in April 2010, initially in a square with 20 km side length (Fig. 2b). The GPS buoy array allows the quantification of the mechanical ice divergence and convergence, so that we can analyze how mechanical opening of the ice pack influenced the prominent ice reduction in the Eurasian Basin during the summer 2010 through the ice albedo-feedback.

In addition to POPS and ITP#38, we analyzed the oceanographic data from another ice-based profiling system, ITP#37, that was deployed in open water area, offshore from the Laptev Sea Shelf, on August 30, 2009. Note that it was deployed in the previous summer than the other two profilers. The ITP#37 moved toward the north from late summer 2009 to spring 2010 with the Transpolar Drift Stream, indicating that the markedly reduced-ice region in the central Eurasian Basin was composed principally of the first year ice rather than perennial ice floes coming from the North Pole region. The data from ITP#37 is compared with those from POPS and ITP#38 by focused on the difference between first year and multiyear ice floes that the instruments deployed on.

We describe methods and data that we used in Section 2. In Section 3, our findings from the oceanographic data obtained by the instruments are presented from a view point of the under-ice mixed layer properties. In this section, we also present a quantitative discussion of ice melting in the regions on the basis of the ocean-to-ice heat fluxes estimated for each oceanographic profiler. Furthermore, we assess an impact of a low pressure system that persisted over the central Eurasian Basin in August to the reduced ice concentration in the basin. Section 4 summarizes the paper.

2 Data and Method

The POPS instrument was deployed at 89.28°N, 89.66°E on April 15 in 2010 by JAMSTEC near Russian ice camp, Barneo (http://www.barneo.ru/index.htm). The POPS consists of a surface-unit that was mounted on multi-year ice of ~ 1.9 m thickness and an underwater profiling float. Sensors equipped with the surface-unit collected data of air temperature and barometric pressure at approximately 1 m height with 1 hour time interval. The oceanic profiling float acquired temperature, conductivity (salinity) and pressure in a depth range of 5–575 m, where the temperature and conductivity sensors are SBE 41CP CTD sensors from Sea-Bird Electronics with an accuracy of 0.005 psu and 0.002°C, respectively. The POPS gathered oceanographic data when the underwater profiler ascends from the greatest depth, with approximately 1.0-2.0 m of vertical resolution, and the oceanographic sampling is performed one-way each day. For the full description of POPS, refer to Kikuchi et al. (2007). The POPS terminated its oceanographic data transmission on August 28 when it was located at 85.11°N, 4.99°E over the Nansen-Gakkel Ridge and north of the Yermak Plateau.

The ITP#38 was deployed on a 1.7 m thick ice-floe in the Transpolar Drift Stream on April 19, 2010 at 88.65°N, 145.60°E, approximately 150 km away from the POPS (see Fig. 2). ITP#38 gathered temperature and salinity data at about 25 cm vertical resolution on four profiles per day from about 7 m depth to about 750 m, and transmitted the data via Iridum satellite (data are taken from the ITP web site, http://www.whoi.edu/itp/data). The ITP underwater profiler cycles vertically along the tether. ITP#37 was deployed on August 30, 2009 in open water at 81°55.7N, 120°10.1E in the Transpolar Drift. The instrument was deployed in collaboration with the Nansen and Amundsen Basins Observational System (NABOS) project from I/B Kapitan Dranitsyn. The ITP#37 was operating on a typical sampling schedule of 2 profiles between 7 and 760 m depth each day. The detailed ITP calibration procedures are described by Johnson et al. (2007).

Four GPS ice drifters were deployed on April 15, 14 km to the north, south, east and west of the POPS. Each buoy consists of a GPS receiver and Iridium modem, transmitting near-real time geographic position with 10 minute time interval. Ice velocity and its spatial gradients (strain rate) were estimated from the temporal and spatial differentials of the hourly interpolated GPS positions using the method of Hutchings and Hibler (2008). The resultant spatial gradients for ice velocity are combined to give time series of ice divergence or convergence, vorticity and shear of the ice motion within the buoy array. The estimated strain rates are valid over the length of buoy array, which is approximately the square root of the buoy array area.

3 Results and Discussion

3.1 Mixed layer properties under the ice

First, we describe hydrographic properties obtained by the POPS and ITP buoys. In the present study, we focus on mixed layer properties such as temperature and salinity since significant changes in that layer most likely affects the ice reduction. Figure 3a depicts temperature and salinity obtained by POPS in the surface layer. During a period between days 110 and 170, the surface mixed layer persisted with a nearly constant depth of ∼50 m, wherein temperature is close to the freezing temperature T_f with an elevation less than 0.1 K than T_f. The mixed layer depth is determined for a minimum depth where density stratification reaches $N^2 = 7\times10^{-4}$ s^{-2}, where N is the Brunt-Väisälä frequency and defined as $N^2 = -\frac{g}{\rho_{w0}}\frac{\partial \rho_w}{\partial z}$ (reference sea-water density ρ_{w0} is 1028 kg m^3 and gravitational acceleration g =9.8 m s^{-2}) (see also Fig. 4). The mixed-layer salinity in the course of the POPS drift was generally less than 32.0 practical salinity unit (PSU), far less saline compared to past observations. This freshening of the mixed layer in the Transpolar Drift Stream during summer 2010 is discussed in Timmermans et al. (2011). They argued that this freshening is attributable to the significant change in atmospheric circulation, leading to the increased volume of freshwater outflow from the Beaufort Sea to join the Transpolar Drift Stream. There is large volume of warm and saltier water underlying the mixed layer, which originates from the North Atlantic Ocean (Swift and Aagaard, 1981; Aagaard et al., 1985).

Figure 5 depicts time series of temperature elevation averaged within the surface mixed layer. The figure shows that ML temperature indicates a moderate increase from day 120 through day 170, and after that, it shows even rapider increase continuing until day 240. During the latter period, the ML temperature increased by 0.3 K, when mixed layer salinity decreased from from 31.4 PSU to 31.2

PSU (Fig. 3a). The depth of strongest stratification representing the mixed layer depth markedly shoals up from 50 m to <20 m (Fig. 4a). This shoaling coincidentally happens when the buoy transects the N-GR. Additionally, it is noteworthy that another maximum of stratification is found after day 180, which is centered at a depth of ∼25 m, shallower than the principal mixed layer of ∼50 m. The two layers with N^2 maximum appear to merge together after day 200 when the lower layer shoals up following the bottom relief of N-GR.

The dual layering structure of mixed layer under the POPS is also found for the ITP#38 (Figs. 3b and 4b). The base of the lower mixed layer shoaled up as the buoy moved across the N-GR (Fig. 4b), as found along the POPS track. The shallower mixed layer whose depth is ∼25 m appears to be associated with the surface water freshening, where salinity decreases from 31.8 to 30.6 PSU between days 170 and 245. ITP#38 recorded the rapid warming in ML temperature after day 170 as well as the POPS did.

Mixed layer properties under ITP#37 are significantly different from those for the other two buoys that were deployed on the multiyear ice (Figs. 3c and 4c). ITP#37 indicates that salinity before the mid-summer was between 33.3–33.5 PSU and much higher than ∼31.5 PSU for POPS and ITP#38. Upper layer temperature is persistently close to T_f. The N^2 plot displays that the mixed layer depth is ∼50 m before day 200 similar to those for POPS and ITP#38, while its stratification at the base is much weaker, where typically $N^2 < 3\times10^{-4}$ s^{-2} (Fig. 4c), than that for the other two. Around day 200, the mixed layer appears very shallow, whose depth is less than 15 m and whose stratification is even stronger than that for the deeper mixed layer during spring time. At the same time, ML temperature dramatically increases, attaining its peak of ∼0.6 K above T_f around day 205; it then decreases rapidly until day 215 (Fig. 5a). The shallow mixed layer is also marked by low salinity water which is less than 0.4 PSU compared to that before day 200.

This abrupt emergence of the shallow mixed layer under ITP#37 would be explained by the same mechanism that the shallower N^2 maximum established under the ITP#38 and POPS since they almost coincidentally occurred within a short period, day 200–210. Namely, fresh melt water was presumably released to the water surface at the timing, producing a highly stratified halocline at such shallow depth. The warm, fresh water within the layer support this hypothesis. Images from web cameras co-located with the buoys also supports this, which recorded that the upper surface of ice floes started to melt after the end of June and form numerous melt ponds overall the surface (http://www.arctic.noaa.gov/gallery_np.html).

The N^2 plot in Figure 4c illustrates that the shallow halocline becomes deeper with time, which is <10 m around day 200 while it becomes ∼30 m by day 240. In general, the surface boundary layer is subjected to an influence of turbulence excited by the surface momentum input, so that it becomes deeper through the erosion process at the base. Thus, the ice motion can stir up waters within the shallow halocline, eventually contributing to the deepening in the mixed layer. The wind-driven mixed layer is known to be modeled in terms of surface friction velocity u_{*0} and stratification N^2 by a following formulation (Cushman-Roisin, 1994):

$$h_{ML} = \left(\frac{12 m u_{*0}^3}{N^2} t \right)^{1/3} + h_{ML0}, \tag{1}$$

where h_{ML} is the mixed layer depth, h_{ML0} is that for the initial time, and a coefficient m is 1.25 based on laboratory experiments. We applied Equation (1) to the cases of POPS, ITPs#38 and #37 (dashed red curves in Fig. 4), where we take $N^2 = 0.5\times10^{-3}$, 0.8×10^{-3}, and 2.0×10^{-3} s^{-2}, and $u_{*0} = 0.005$, 0.007 and 0.006 m s^{-1}, respectively, on the basis of the observation (see also Fig. 6). Please refer to the full description below for the u_{*0} estimation. In Figure 6, the theoretical curves capture well the observed temporal evolution in the surface mixed layer depth. That is, the weaker (stronger) stratification due to the fresh melt water is eroded by turbulence, producing the deeper (shallower) mixed layer with time. Consequently, we can explain that the rapid dissipation of the high temperature within the shallow surface layer under the ITP#37 is due to the convective motion stirred by the surface turbulence (Fig. 3c). It is interesting that the high temperature still remains only at the base of mixed layer.

3.2 A bulk estimate for oceanic heat flux

In the present section, ocean-to-ice turbulent heat flux is estimated based on the parameterization developed by McPhee (1992). It is formulated as follows:

$$< w'T' >_0 = \rho c_p c_H u_{*0} \delta T, \tag{2}$$

where c_p =3980 J kg^{-1} is the specific heat of sea water, c_h =0.0057 is a heat transfer coefficient (see McPhee et al., 2003), and δT is the difference between temperature in the well-mixed boundary layer and freezing temperature T_f that is a function of mixed-layer salinity. Density of sea water ρ is 1028 kg m^{-3}, and u_{*0} is the interfacial friction velocity between ice and ocean.

The friction velocity $\mathbf{u_{*0}}$ is estimated from ice-drift velocity $\mathbf{U}$ using a Rossby similarity relationship (see McPhee, 2008 for further explanation)

$$\frac{\kappa \mathbf{U}}{\mathbf{u_{*0}}} = \log \frac{|u_{*0}|}{f z_0} - \alpha - i\beta, \tag{3}$$

where $\mathbf{u_{*0}}$ and $\mathbf{U}$ are expressed as complex number, κ =0.4 is von Karman's constant, and f is the Coriolis parameter with constants α =2.12 and β =1.91. For the hydraulic roughness of the ice undersurface, we take z_0 =0.01 m as used in Timmermans et al. (2011) and many past studies. Also following McPhee (2003), we removed inertial components from $\mathbf{U}$ using a 12-hour running mean which is based on the evidence that the inertial component of shear at the ice-ocean interface can be neglected because the ice and upper ocean react in the same way to the forcing.

Figure 6 plots the magnitude of friction velocity estimated from Equation (3). According to Figure 6, the three ocean profiling buoys show similar behaviors in friction velocity which is principally due to the variability in ice speed. They exhibit moderate fluctuations with periods of 3–5 days until day 180. Meanwhile, friction velocity drastically changed into vigorous fluctuation after day 200, most of which have relatively short-term oscillation which is removed by the running-mean procedure. Hence, it does not affect result of the heat flux calculation presented below.

Wavelet analysis of ice velocity, divergence, shear and vorticity provides further detailed insight regarding the ice motion in the vicinity of POPS (Fig. 2b). The wavelet analysis is applied to the buoy array strain rate components, following Grinsted et al. (2004), using a 6^{th} order morlet wavelet. The results, for vorticity (curl of the velocity field resolved by the GPS buoy array), are plotted in Figure 7. The figure shows that the vorticity of sea-ice motion stays generally quiet through day 200. After that, it becomes much more vigorous in the semi-diurnal tidal/inertial band at frequencies of 2.0–2.1 cycles per day (CPD), which is close to the local inertial frequency (2.08 CPD). After day 200, the variation is also pronounced at low frequencies of 0.1–0.5 CPD as well as exhibiting a relatively high frequent inertial motion. After day 260, the intensified oscillation at $\sim$2 CPD still persists although it becomes intermittent. The overall features described above are found for ice velocity, divergence and shear as well. Excitation of ice motion in the inertial band is indicative of an ice pack that has become weakened, with reduced internal ice interaction (Colony and Thorndike, 1980; Geiger and Perovich, 2008).

The ocean-to-ice heat flux is depicted in Figure 5b. The oceanic heat flux starts to increase on day 170, commonly among the three buoys. ITP#37 indicates the most rapid increase and the earliest attainment of its maximum, >70 W m^{-2}, around day 200–210. This $< w'T' >_0$ value estimated for ITP#37 is much larger compared to earlier studies for similar downcurrent regions of Transpolar Drift Stream, i.e. Eurasian Basin, Greenland Sea, and so on (Krishfield, et al., 2005). For example, it is estimated to be <20 W m^{-2} in McPhee et al. (2003) and $\sim$40 W m^{-2} at maximum in Maykut and McPhee (1995) by the same method. After day 210 $< w'T' >_0$ exhibits monotonic decrease with time except for maxima at day 230 until it becomes a nearly zero flux around day 250. Regarding POPS and ITP#38, temporal variation in $< w'T' >_0$ largely coincide with each other during melt season starting on day 170 and increasing with time until the end of the melt season around day 245. Interestingly, the heat flux after day 200 appears to be greater on average, relative to the period until then. This is presumably due to the generally higher level of u_{*0}, representing faster ice movement because of the reduced internal ice friction during the melt season (Fig. 6). The changes in mixed layer stratification such as the surface layer freshening and shoaling may also contribute to the enhanced ice motion partially (Kawaguchi and Mitsudera, 2008).

The turbulent heat flux can be converted into temporal evolution in ice thickness assuming that all of the heat is used for fusion at the undersurface of the ice. Namely, it is expressed by the following relationship:

$$L_f \rho_i \frac{\partial h}{\partial t} = < w'T' > = c_w \rho_w u_{*0} \delta T, \tag{4}$$

where L_f is the latent heat of fusion for sea ice and L_f =0.276 MJ kg^{-1}, and ice density ρ_i is 910 kg m^{-3}. A variable h denotes ice thickness as a function of time. Integrating Equation (4) from the beginning of the melt season gives the cumulative amount of ice ablation at the undersurface. Figure 5c shows the accumulated volume of ice melt for the three ITP and POPS buoys. As expected, ITP#37 exhibits the fastest ice ablation and largest accumulated volume of melt than the other two buoys. The ice melt begins to increase on day 170 and then rapidly accelerates at day 200. After that, it returns to the modest increase lasting throughout August and early September in 2010 (days 220–250). The total ice melt for the ITP#37 is estimated to be 1.6 m over three months during the melt season. In contrast, the accumulated ice volume for ITP#38 is estimated at roughly 80 cm. Although POPS terminated the oceanographic transmission around day 240, it still estimates about 70 cm melt until the end of August.

Timmermans et al. (2011) evaluated the actual changes in ice thickness on the basis of ice mass balance (IMB) buoy that was deployed adjacent to ITP#38. They show that the ice thickness decreased by approximately 40 cm between days 170 and 250 during summer 2010. Perovich et al. (2008) presents their estimates for the ice melt using IMB deployed near the North Pole for several years since 2000. In their estimate, ice bottom melt is less than 50 cm in annual amount for 6 years between 2000 and 2007, which is roughly comparable to the estimate for summer 2010 by Timmermans et al. (2011). Our estimate for the thickness change differs from these IMB observations approximately by a factor of two. Source of this might be explained by the fact that we assumed that all of heat emitted from ocean is consumed for the ablation at ice bottom surface as expressed in Equation (4). However, a part of heat flux from the water can penetrate into the ice interior.

3.3 Impacts of a low pressure system

Ice (buoy) motion vorticity was abruptly enhanced after day 200 as shown in Figure 7. The divergence/convergence rate derived from the GPS buoy array indicates a prominent enhancement in amplitude as well (Fig. 8a). According to Figure 8a, the prominent events of ice divergence occurred several times from the end of July to mid-August. Figure 8b shows that the temporal variation in buoy area has a pronounced buoy array expansion around day 225. The area was persistently 300 km^2 before day 200, then it is enlarged up to almost 500 km^2 which is nearly 1.7 times greater than before.

Ice concentration change due to divergence and convergence of the ice pack (which we refer to as mechanical ice concentration), can be simply estimated by $C_*(t) = A_0/A(t)$, where $C_*(t)$ is the mechanical ice concentration as a function of time t, and $A(t)$ is buoy array area. A_0 is the initial buoy-array area, which is the minimum area of the buoy array in the week after deployment. The concentration decreases as ice area increases relative to the initial area. Additionally, the concentration is limited to be C_* =1 for $A_0/A \geq 1$, indicating pressure ridge formation under the convergent motion implicitly. Initially, we assume a fully packed concentration, i.e., $C_*(t = 0) = 1$. To clarify the importance of ice concentration variation due to mechanical component, SSM/I ice concentration is optimally interpolated along the course of the GPS buoy in the vicinity of POPS. The SSM/I data set is created by the Artist Sea Ice (ASI) algorithm (Erzaty et al., 2007) using the 85 GHz brightness temperature distributed from National Snow and Ice Data Center. The resolution is 12.5 km $\times$ 12.5 km horizontally and daily temporally.

In Figure 8c, the mechanical ice concentration C_* is plotted in time series, together with the SSM/I concentration C. The SSM/I indicates that C has a minimum of $\sim$85% around days 190–200, and then it recovers to >95% by day 210. It afterward decreases attaining its lowest minimum of 65% around day 227, which is preceded by the greatest ice divergence between days 220–226 (shaded in Fig. 8b). After the marked divergence event, the buoy array showed a closing motion, so that the mechanical concentration promptly recovers up to 100% by day 230. In the period, the SSM/I concentration appears to follow the increase in mechanical concentration, but it reaches only less than 90%. This discrepancy in ice concentration restoration would be explained as follows. While the strong ice divergence during the mid-August forcibly exposes some fraction of open water to the air, the solar radiation is increasingly deposited at the surface layer water through the resultant lead area, which causes lateral melt. Hence, on closing by the amount that the pack had opened, the mechanical concentration returns to 100% although the actually concentration is lower due to ice melt. After that, the SSM/I concentration restores to 100% in a brief period of days 245–260 when air temperature was generally below -10°C then (Fig. 8d) and ML temperature was almost equivalent to T_f according to the hydrographic data (Figs. 3b and c). Therefore, the rapid restoration in ice concentration in the early September can be attributed to freezing of seawater at the open water fraction.

We think that the ice concentration reduction in the mid-August is related to a synoptic-scale atmospheric circulation. Figure 9 shows mean sea level pressure (SLP) over the period between days 220–226 when strong divergence was recorded by the GPS buoys (shaded in Fig. 8b). The figure shows that the extensive low pressure system covered the central Arctic Ocean and the overall Eurasian Basin. Under the system, sea level pressure was $<$1003 hPa near the center and $\sim$1014 hPa along the outer edge of the low. It also shows that the POPS and GPS buoy array were located very close to the center of low pressure system (denoted by a square). The map of SSM/I ice concentration displays horizontal pattern of ice concentration changes over the period of days 220-226 when the low pressure persisted. According to the image, the concentration was lowered greatest at the center of the low pressure system, resulting in as much as 30–40% reduction. However, the decrease in the concentration is not necessarily in a symmetry with respect to the center of the low; besides the greatest reduction in the center of the low, it is also substantial at marginal ice zones extending to the Severnaya Zemlya and to the east of Greenland through the Fram Strait from the low's center.

Numerous earlier studies (e.g., Thorndike and Colony, 1982; Serreze et al.,

1989) have examined ice divergence and decrease in ice concentration driven by cyclonic atmospheric circulation. Serreze et al. (1989) proposed a two-dimensional regression model for ice divergence which is based on sea level pressure and geostrophic wind with constants D_0 and θ that are estimated for each season. Here, we assess how rapidly ice diverges under the low pressure system, following Serreze et al. (1989):

$$
\begin{aligned}
\nabla_H \cdot \mathbf{U} &= D_0 \sin\theta\left(\frac{\partial W_y}{\partial x} - \frac{\partial W_x}{\partial y}\right) && (5)\\
&= -f D_0 \sin\theta \nabla^2 \Psi && (6)
\end{aligned}
$$

where W_x and W_y respectively denote meridional and zonal velocities of geostrophic wind, defined by $W_x = \frac{1}{f}\frac{\partial\Psi}{\partial y}$ and $W_y = -\frac{1}{f}\frac{\partial\Psi}{\partial x}$ using the geopotential Ψ and the Coriolis parameter f. Mathematical operator $\nabla_H\cdot$ denotes horizontal divergence for vector variables. The constants D_0 and θ are 0.0105 and 18°, respectively, which are proposed by Thorndike and Colony (1982) who determined these values on the basis of a number of buoy motion for cyclone activities for the melt season. With regard to the wind velocity (W_x, W_y), we chose wind at a pressure level of 925 mbar on which level geostrophic balance is assumed. The wind data is extracted from Japanese 25-year Re-Analysis (JRA-25) (Onogi et al., 2007) which is 1.125° in spatial resolution and 6 hours in time interval. Equation (5) physically means that the ice divergence varies proportional to relative vorticity of the geostrophic winds. Consequently, the divergence is also expressed by the Laplasian form for the geopotential Ψ as in Equation (6), so that it has its maximum at the trough of SLP contours because sea level pressure can be viewed as a function of Ψ in the polar region where f is nearly constant.

Based on Equation (5), $\nabla_h \cdot \mathbf{U}$ is computed and averaged for 7 days during the period of days 220–226. The results are plotted in Figure 10 and demonstrate that the low pressure system drives divergent motion that is greatest in the Eurasian

Basin, and appears generally consistent with the spatial variation in ice concentration change derived from SSM/I (Fig. 9). In more detail, it evaluates the largest divergence at the center of SLP minimum. It also depicts the ice divergence maximums at the regions that extend toward the Severnaya Zemlya and toward the Geenland Sea from the center of the low. This keeps consistency with the analytical prediction of Equation (6) where the divergence yields along the troughs of SLP contours. An exception to be noted is the coastal region north of the Greenland, which is located along a trough of SLP contours where the ice divergence is predicted to be considerable. However, the observation shows an opposite tendency in ice concentration – a slight increase. This is probably because sea ice motion toward the coast, following the winds, and consequently ice-ice interaction prevented divergence.

In more quantitative discussion, ice divergence due to the low pressure system is estimated less than 10% in the center at most, whereas ice concentration reduces to 30% during the same period. The discrepancy is also argued in Serreze et al. (1989). In the paper, the numbers of buoy motion have exhibited ice divergence typically less than 1% per day under cyclone. Meanwhile, satellite-based ice concentration represents that the associated reduction in ice concentration is even greater, e.g. 20 %. Our buoy array, initially in a 20 km-sided square, was located almost right at the center of the cyclone, which shows quantitatively much better agreement with the variation of SSM/I concentration (Fig. 8c). The constants $D_0 = \sim 0.01$ and $\theta = \sim 20^\circ$ proposed in the earlier studies are based on sparsely distributed buoys motion (typically >100 km in distance). We thus suggest that they need to be updated including a large number of samples with highly distributed buoys.

4 Summary

This study examines ice reduction in the central and eastern Arctic Ocean during summer 2010 using ice-based autonomous buoy systems that collect temperature and salinity under the ice. Based on the oceanographic data, the estimation of ocean-to-ice heat flux and undersurface ice ablation indicates significant spatial differences between fluxes in first-year and multi-year ice regions. The oceanographic instrument ITP#37 that drifted with the first-year ice exhibits significantly high ML temperatures reaching 0.6 K elevation relative to T_f, allowing >60–70 W m^{-2} of heat flux emitted to the ice. In contrast, the POPS and ITP#38 that were deployed on the perennial ice floes show that the oceanic heat flux is equivalent to 40 W m^{-2}, corresponding to accumulatively 0.8 m of ice melt over three months. Additionally, the wavelet analysis of sea ice motion shows the abrupt enhancement after day 200 in each component of strain rate. The enhanced ice motion is characterized by a specific periodic band of inertial/semidiurnal tidal oscillations.

We also found that ice concentration was significantly reduced associated with a persistent low pressure system in the mid-August. The low pressure system laid for a week over the Nansen and Amundsen Basins, where our GPS buoys recorded marked ice divergence under the central region of the low and at troughs of the sea level pressure. The SSM/I images shows that low ice concentration continued throughout August even after the low dissipated. This suggests that the divergent ice motion driven by the cyclone led to increased absorption of incident solar radiation in the surface water, resulting in the further sea ice melt due to the increased ML temperature.

Acknowledgements

The instruments used in this study were deployed in collaboration with the North Pole Environmental Observatory (NPEO) from the Russian Barneo ice camps with logistic support provided by Andy Heiberg from Polar Science Center (University of Washington) and Tom Quinn. We appreciate Dr. Pisarev and T. Noguchi of MWJ for their deployment support. We also thank two anonymous reviewers whose comments improved the content and clarify of this manuscript. The Ice-Tethered Profiler data were collected and made available by the Ice-Tethered Profiler Program based at the Woods Hole Oceanographic Institution (http://www.whoi.edu/itp). JAMSTEC supported this study. National Science Foundation is acknowledged for NPEO and ITP support.

References

Aagaard, K., Swift, J. H., Carmack, E. C., 1985. Thermohaline Circulation in the Arctic Mediterranean Seas. J. Geophys. Res., 90, C3, 4833–4846.

Colony, R., Thorndike, A.S., 1980. The horizontal coherency of the motion of summer Arctic sea ice. Journal of Physical Oceanography 10 (8), 1281–1289.

Cushman-Roisin, B., 1994. Introduction to Geophysical Fluid Dynamics. Prentice-Hall, Inc., New Jersey, pp. 320.

Ezraty, R., Girard-Ardhuin, F., Piollé, J. F., 2007. Arctic and Antarctic sea ice concentration and Arctic sea ice drift estimated from special sensor microwave data–User's manual.

Grinsted, A., Moore, J. C., Jevrejeva, S., 2004. Application of the cross wavelet transform and wavelet coherence in geophysical time series. Nonlinear Proc. Geophys., 11(5-6), 561-566.

Geiger, C. A., D. K. Perovich, 2008. Springtime ice motion in the western Antarc tic Peninsula region, Deep-Sea Research II, 55, 338-350.

Hutchings, J.K., Hibler III, W. D., 2008. Small-scale sea ice deformation in the Beaufort Sea seasonal ice zone. J. Geophys. Res., 113, C08032, doi:10.1029/2006JC003971.

Johnson, G. C., Toole, J. M., Larson, N. G., 2007. Sensor Correction forSea-Bird SBE-41CP and SBE-41 CTDs. J. Atmos. and Ocean. Tech., 24, 1117-1130.

Kawaguchi, Y., Mitsudera, H., 2008. A numerical study of ice-drift divergence by cyclonic wind with a Lagrangian ice model. TELLUS, DOI: 10.1111/j.1600-0870.2008.00321.x.

Kikuchi, T., Inoue, J., Langevin, D., 2007. Argo-type profiling float observations under the Arctic multiyear ice. Deep Sea Res. I, 54, 9, 1675-1686.

Krishfield, R. A., Perovich, D. K., 2005. Spatial and temporal variability of oceanic heat flux to the Arctic ice pack. J. Geophys. Res., 110, C07021, doi:10.1029/2004JC002293.

Krishfield, R. A., Toole, J., Proshutinsky, A., Timmermans, M.-L., 2008. Automated Ice-Ththered Profilers for seawater observation under pack ice in all seasons. J. Atmos. Ocean. Technol., 47(11), 2091-2015.

Maykut G. A., McPhee, M. G., 1995. Solar heating of the Arctic mixed layer. J. Geophys. Res., 100, C12, 24,691-24,703.

Mellor, G. L., Yamada, T., 1982. Development of a turbulence closure model for geophysical fluid problems. Rev. Geophys. Space Phys., 20(4), 851-875.

McPhee, M. G., 1992. Turbulent heat flux in the upper ocean under sea ice. J. Geophys. Res., 97, 5365-5379.

McPhee, M. G., Kikuchi, T., Morison, J. H., Stanton, T. P., 2003. Ocean-to-ice heat flux at the North Pole environmental observatory. Geophys. Res. Lett., 30, 24, 2274.

McPhee, M. G., 2008. Air-Ice-Ocean Interaction: Turbulent Ocean Boundary Layer Exchange Processes, Springer.

Morison J. H., McPhee M. G., Maykut, G. A., 1987. Boundary layer, upper ocean, and ice observation in the Greenland Sea marginal ice zone. J. Geophys. Res., 92, C7, 6987-7011.

Onogi, K., J. Tsutsui, H. Koide, M. Sakamoto, S. Kobayashi, H. Hatsushika, T. Matsumoto, N. Yamazaki, H. Kamahori, K. Takahashi, S. Kadokura, K. Wada, K. Kato, R. Oyama, T. Ose, N. Mannoji and R. Taira, 2007. The JRA-25 Reanalysis. J. Meteor. Soc. Japan, 85, 369-432.

Perovich D. K., Light, B., Eicken, H., Jones, K. E., Runciman, K., Nghiem, S. V., 2007. Increasing solar heating of the Arctic Ocean and adjacent seas, 1979-2005: Attribution and role in the ice-albedo feedback. Geophsy. Res. Lett., 34, L19595.

Perovich, D. K., Ritcher-Menge, J. A., Jones, K. F., Light, B., 2008. Sunlight, water, and ice: Extreme Arctic sea ice melt during the summer of 2007. Geophys. Res. Lett., 35, L11501.

Serreze, M. C., Barry, R. G., McLaren, A. S., 1989. Seasonal variation in sea ice motion and effects on sea ice concentration in the Canada Basin. J. Geophys. Res., 94, C8, 10,955-10,970.

Swift, J. H., Aagaard, K., 1981. Seasonal transition and water mass formation in the Iceland and Greenland seas. Deep-Sea Res., 28, 1107–1129.

Thorndike, A. S., Colony R., 1982. Sea ice motion in response to geostrophic winds. J. Geophys. Res., 87, 5845-5852.

Timmermans, M.-L., Proshutinsky, A., Krishfield, R. A., Perovich, D. K., Richter-Menge, J. A., Stanton, T. P., Toole, J. M., 2011. Surface freshening in the Arctic Ocean's Eurasian Basin: an apparent consequence of recent change in the wind-driven circulation. J. Geophys. Res., in press.

Toole, J., Krishfield, R. A., Proshutinsky, A., Ashjian, C., Doherty, K., Frye, D., Hammar, T., Kemp, J., Peters, D., Timmermans, M.-L., von der Heydt, K., Pickard, G., Shanahan, T., 2006. Ice Tethered-Profilers Sample the Upper Arctic Ocean. EOS, Trans. AGU, 87(41), 434, 438.

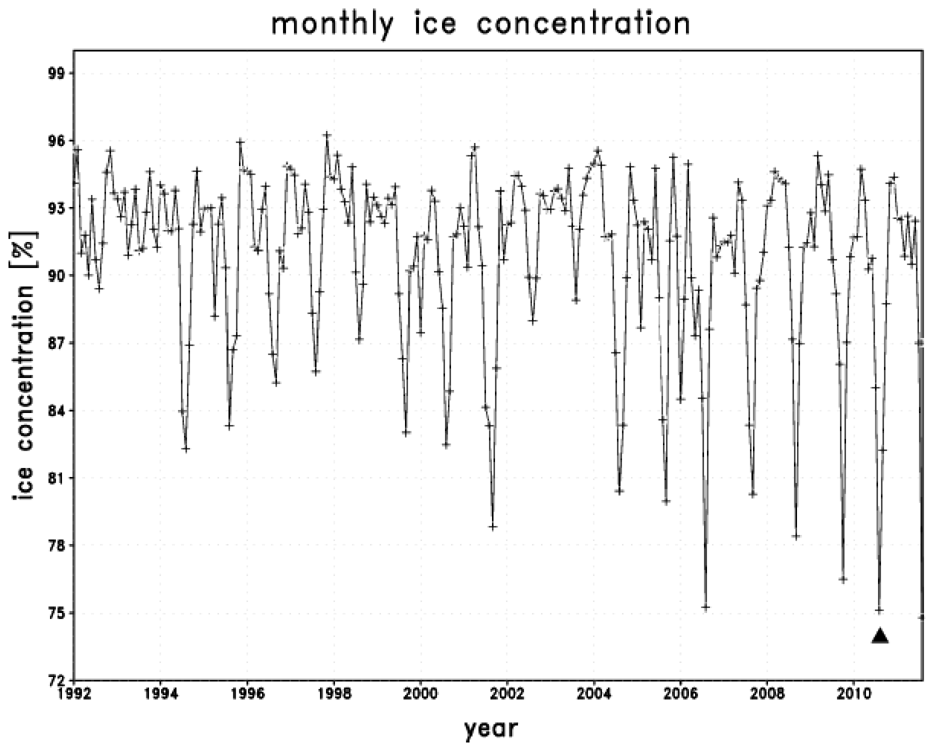

Figure 1: SSM/I ice concentration averaged for the domain denoted in Figure 2. A triangle marks that in August, 2010.

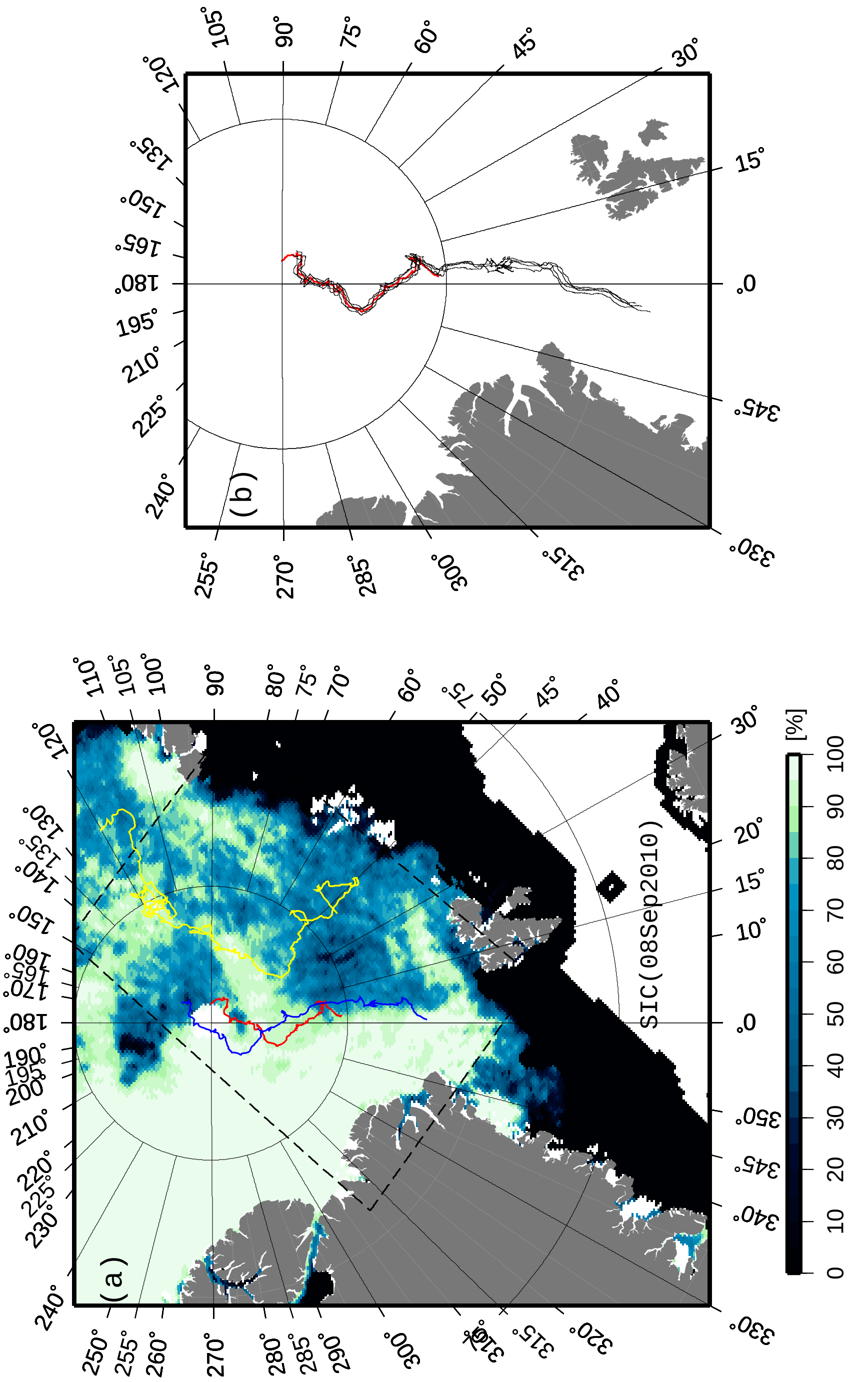

Figure 2: (a) Tracks of autonomous profiling buoys deployed in the mid-April 2010 near the North Pole, which is overlaid with SSM/I ice concentration on September 7, 2010. Curves in colors of red, blue and yellow denote POPS, ITP#38 and ITP#37, respectively. (b) Tracks of four GPS drifters surrounding POPS, which were deployed nearby the North Pole on April 15.

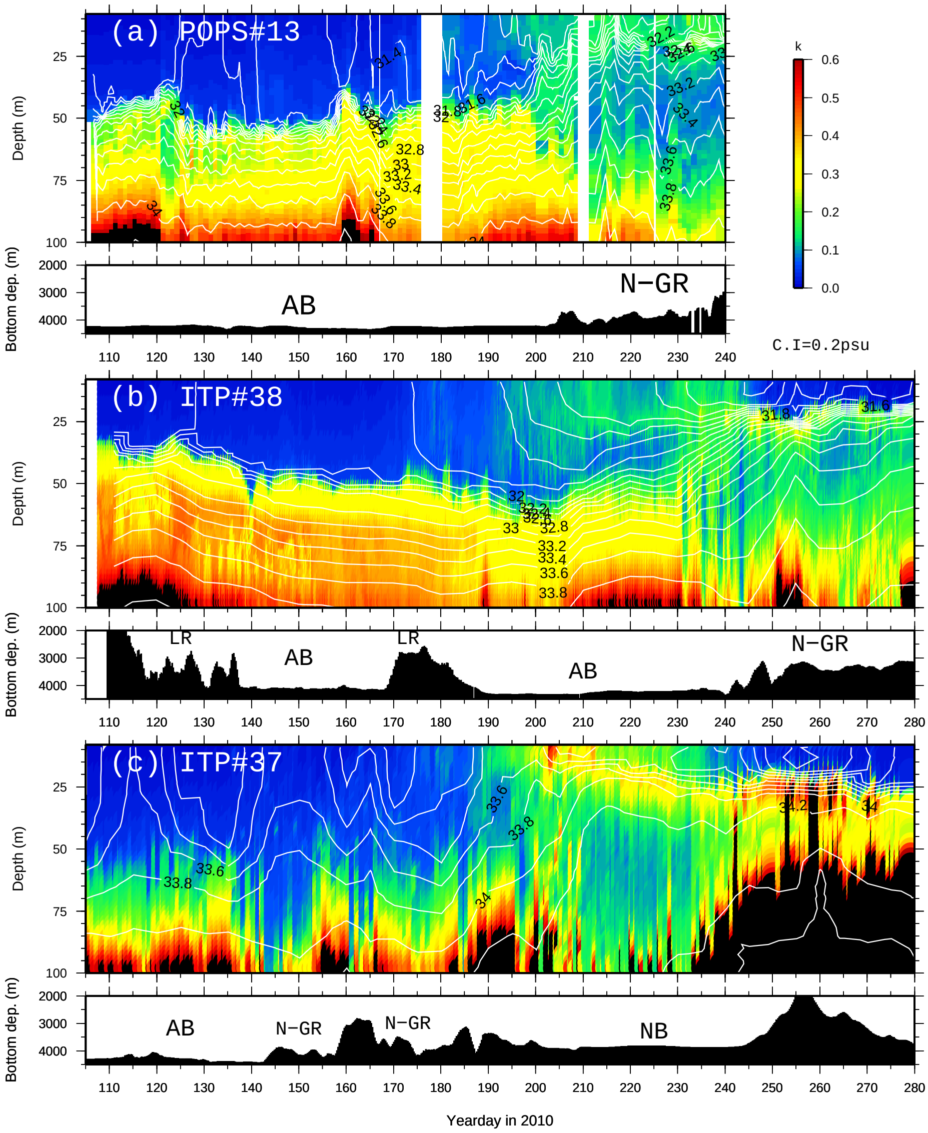

Figure 3: Oceanographic properties of temperature deviation from freezing temperature (color) and salinity (contour) along the course of each buoy: (a) POPS, (b) ITP#38 and (c) ITP#37. Bathymetry along the buoy track is depicted at the bottom of each panel. Acronyms AB, N-GR, NB, and LR denote Amundsen Basin, Nansen-Gakkel Ridge, Nansen Basin, and Lomonosov Ridge, respectively.

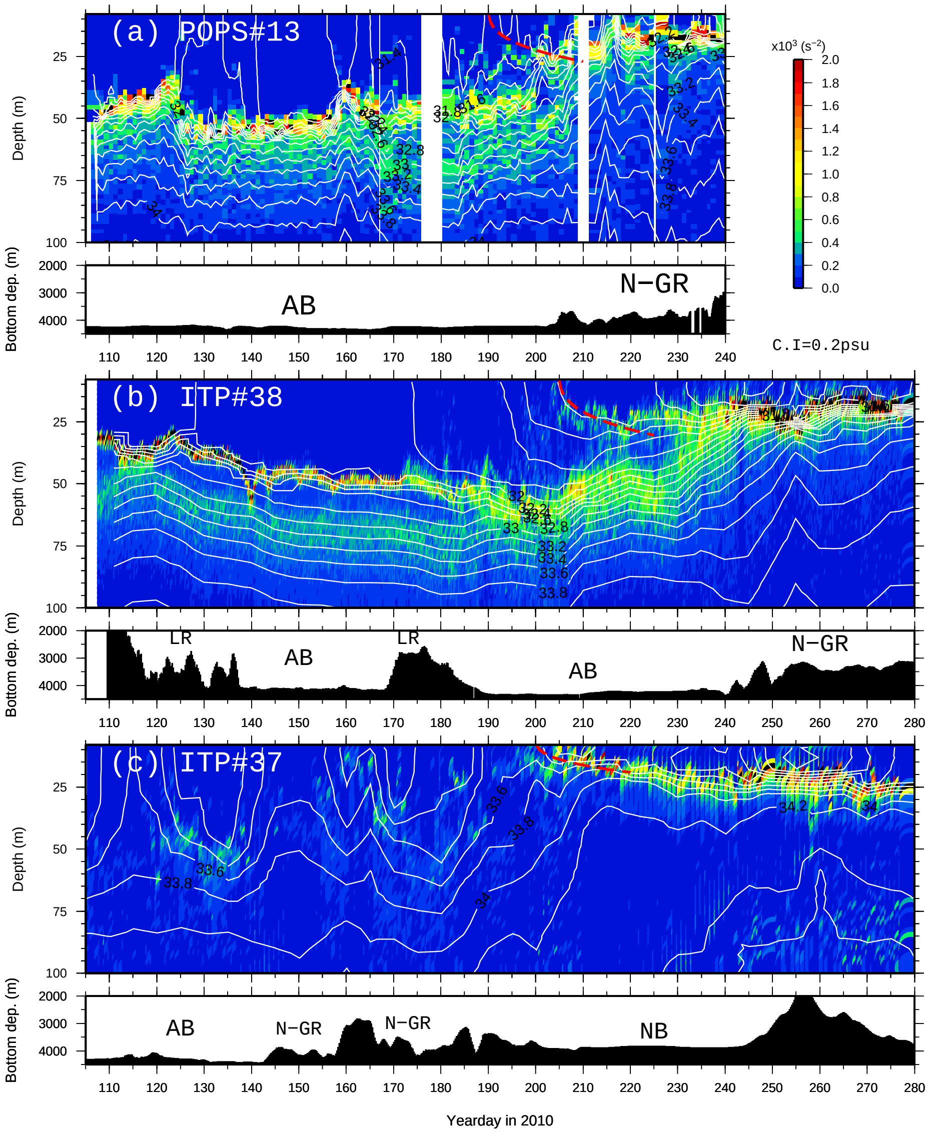

Figure 4: Same as Figure 3 but for Brunt-Väisälä frequency N plotted in color. Dashed red curves on each panel denote the analytical solution (1) by wind-driven mixed layer deepening.

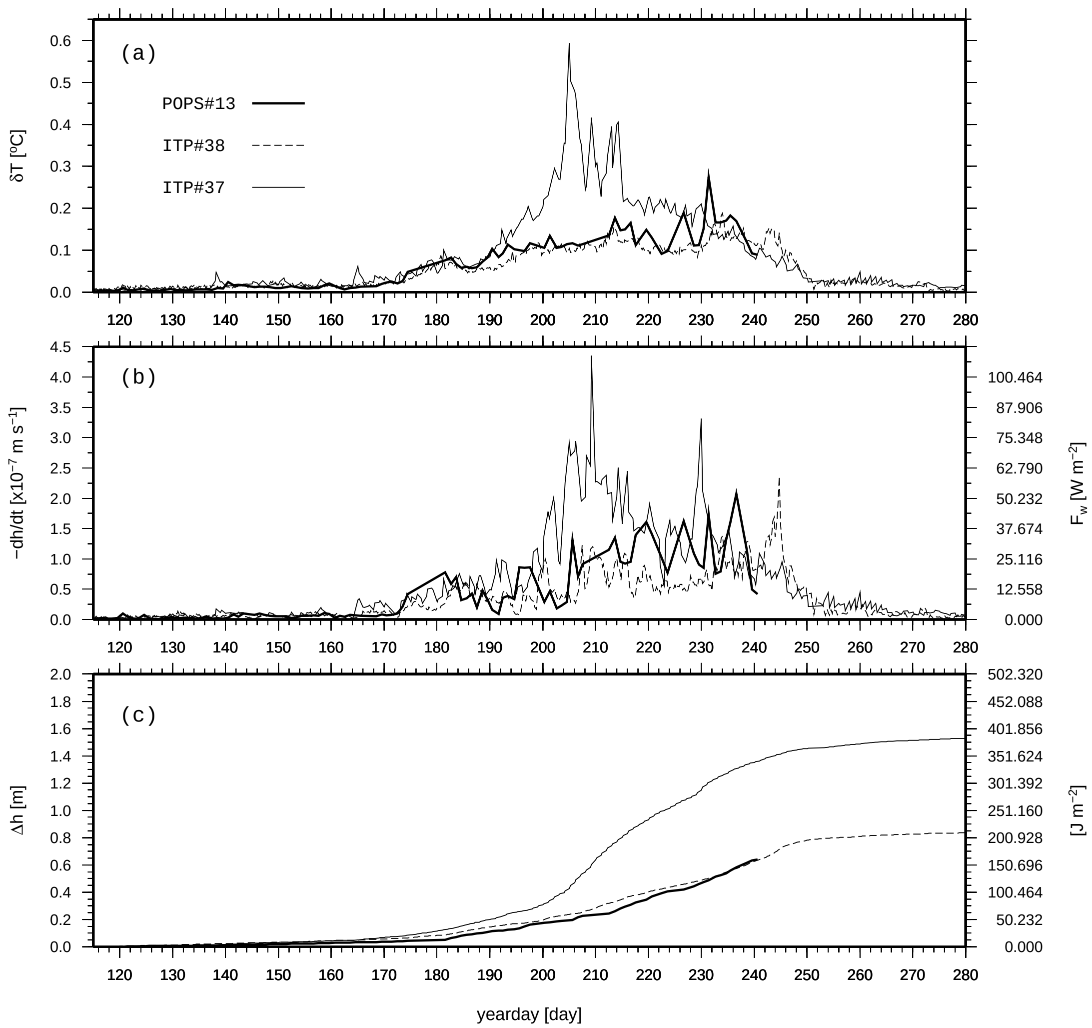

Figure 5: Time series in (a) mixed-layer temperature elevation (K) above T_f, (b) ocean-to-ice heat flux (W m^{-2}), and (c) accumulated ice melt (m). Mixed layer temperature is averaged between surface and a minimum depth where $N^2 = 7\times10^{-4}\ s^{-2}$. It is noted that mixed layer depth is defined by another way before day 200 for (c), where we take a depth with the maximum stratification between surface and 100 m in depth. An estimation of oceanic heat flux is based on Equation (2).

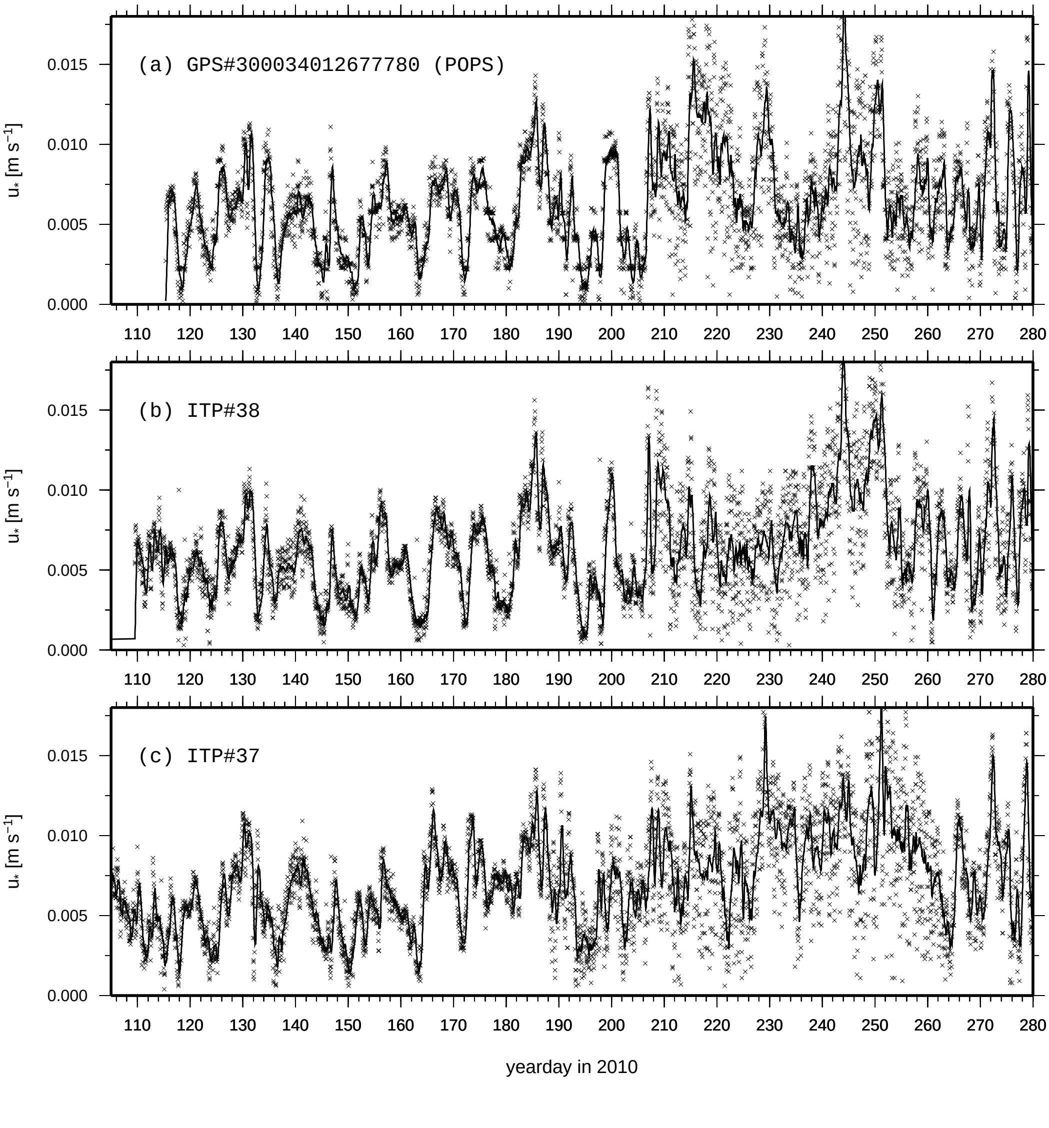

Figure 6: Times series of interfacial friction velocity u_{*0} derived from Equation (3). Raw data is plotted in dot and 12-hours running mean in solid curve. Panels (a), (b) and (c) represent a GPS drifter adjacent to POPS, ITP#38 and ITP#37, respectively.

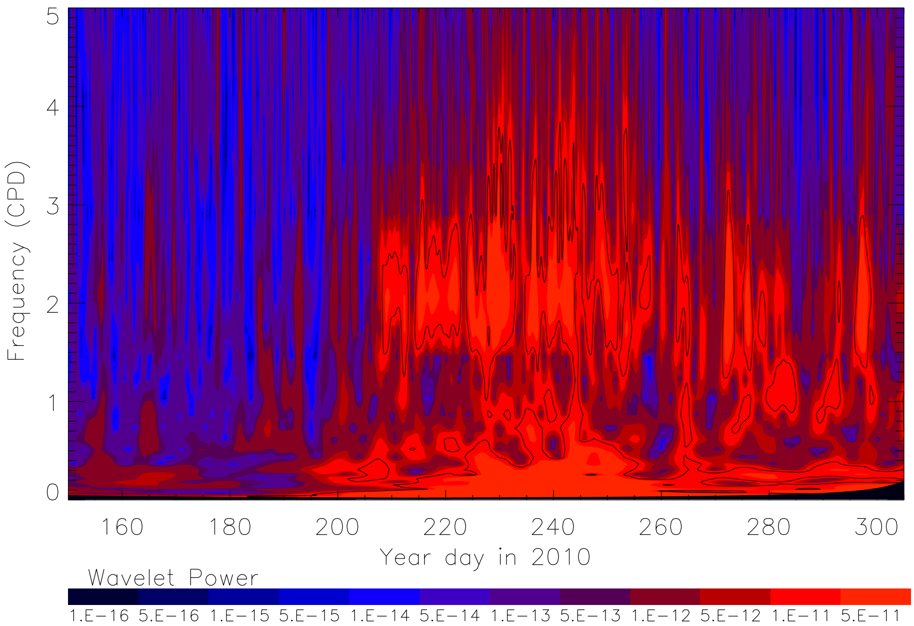

Figure 7: Wavelet power spectrum, using a 6th order Morlet wavelet, of GPS buoy array vorticity, in the 200 to 500 km^2 region defined by the buoy array area surrounding POPS. The cone of influence, below which data should be disregarded, is indicated in solid black. 99% significance levels are plotted at solid lines.

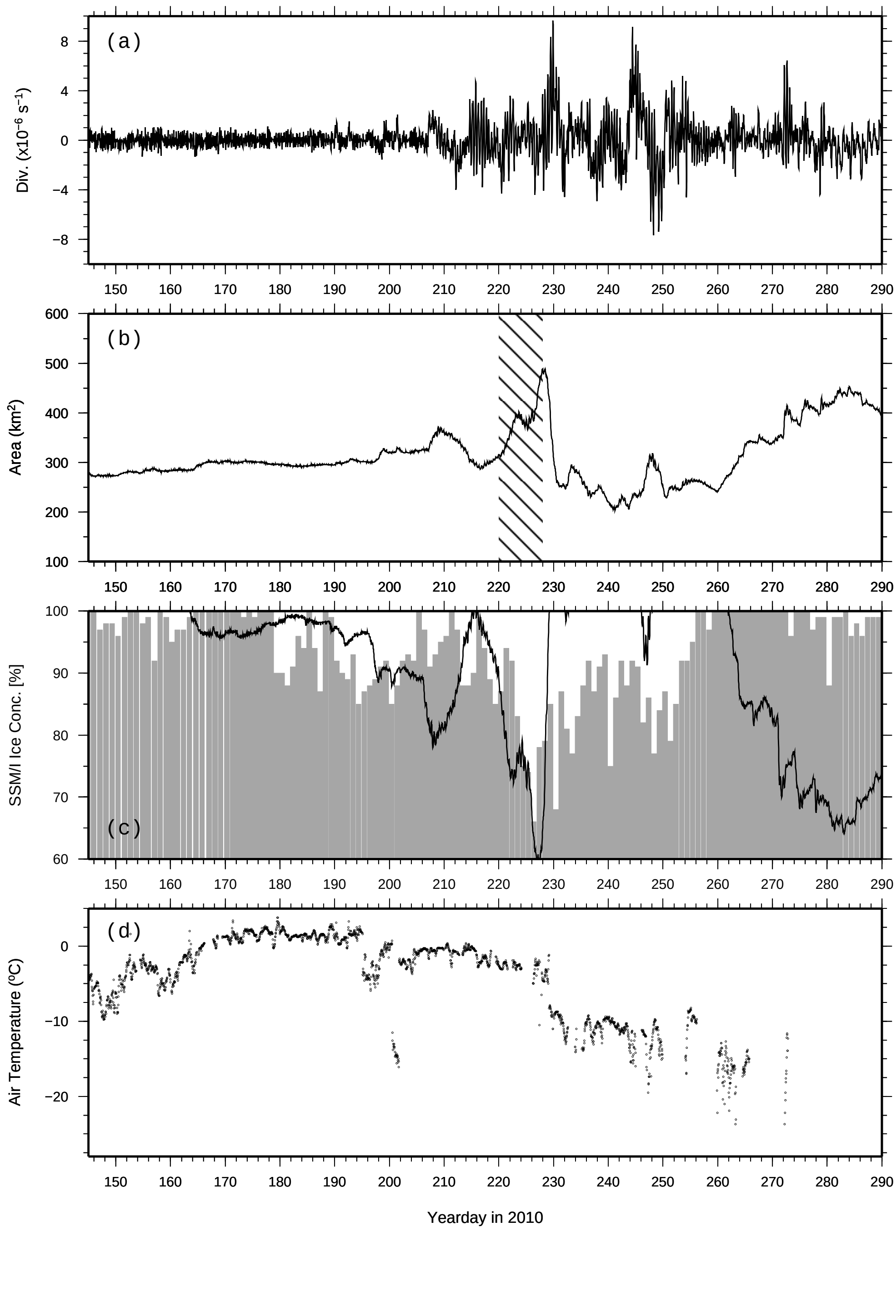

Figure 8: Time series in (a) ice drift divergence (s^{-1}) derived from GPS buoy array, (b) buoy array area (m^2), (c) ice concentration where SSM/I concentration (bars in glay) are derived by ASI algorithm with 12.5 km resolution, and (d) air temperature at 1 m height. In (b), buoy array area is calculated by integrating divergence rate of (a) in time. Further, the hatched region represents a period when the low pressure persisted near the POPS. In (c), ice concentration estimated from mechanical ice divergence is overlaid by a solid curve.

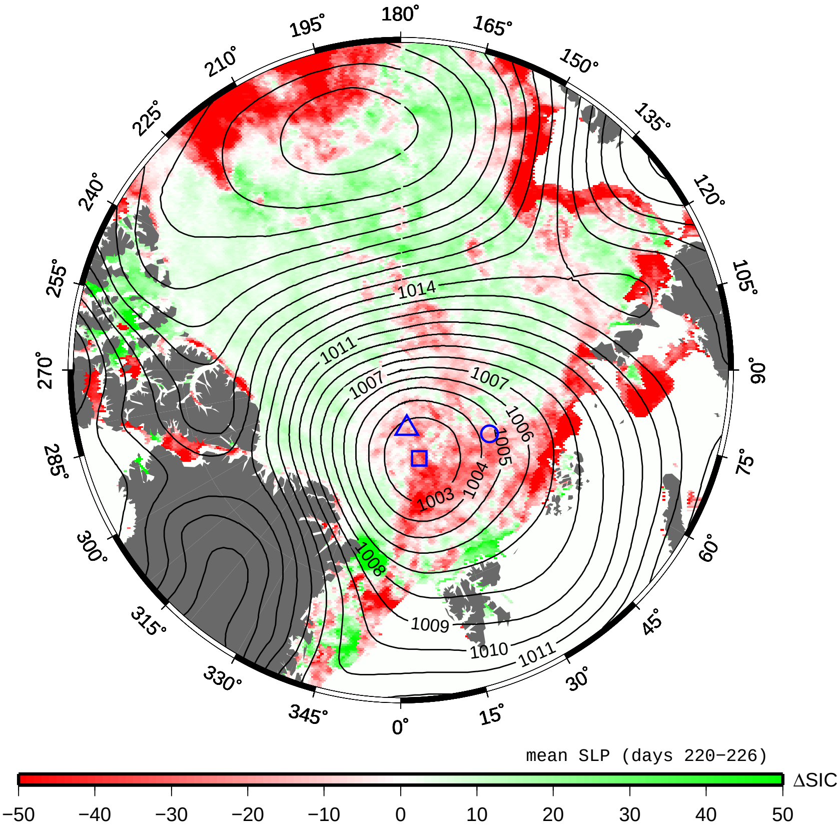

Figure 9: Temporal change in SSM/I ice concentration during days 220–226, superimposed by mean sea level pressure (contour) for the same period. Triangle, square and circle mark respective positions of ITP#38, POPS and ITP#37 on day 225.

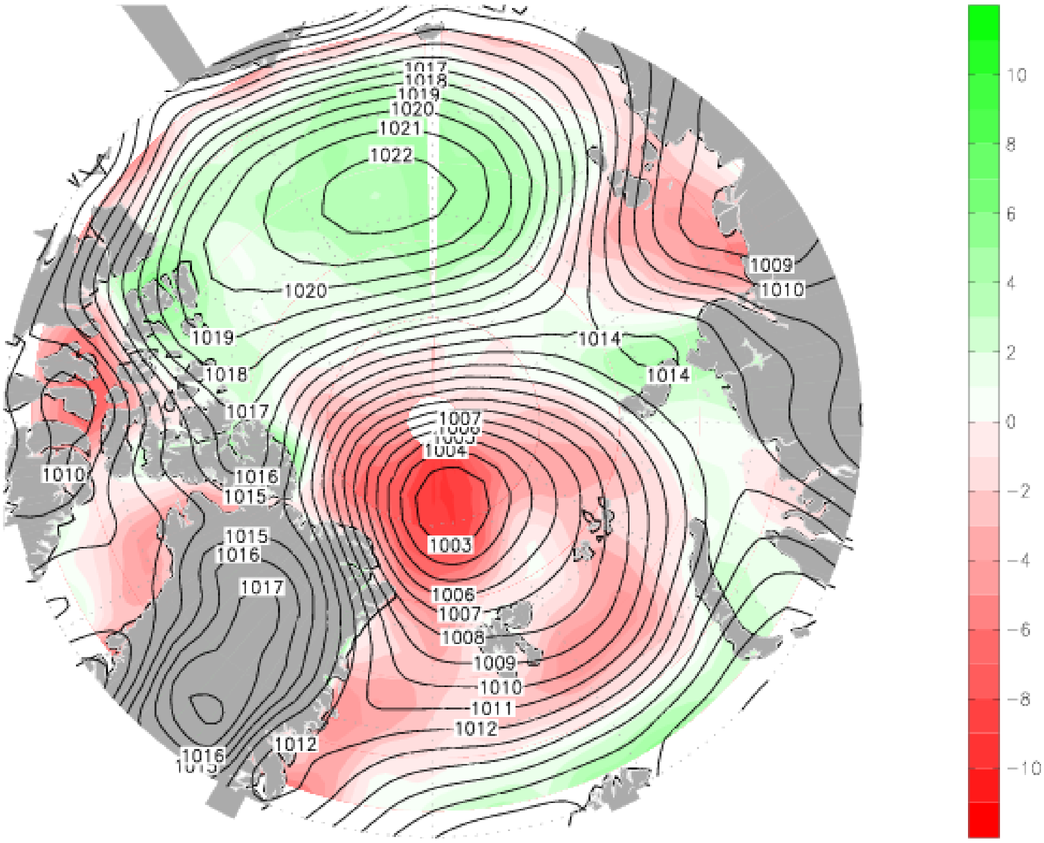

Figure 10: Ice divergence (%) integrated between days 220 and 226, which is estimated by Equation (5) following Serreze et al. (1989). Sea level pressure (hPa) overlays in contour.